Chemical Engineering Science 283 (2024) 119371

Contents lists available at ScienceDirect

Chemical Engineering Science

journal homepage: www.elsevier.com/locate/ces

Modeling pseudo-turbulent heat flux in gas-solid heat transfer

Jiazhong Zhou [a,b], Bo Sun [b,c,d], Shankar Subramaniam [a,b,*]

[a] Department of Mechanical Engineering, Iowa State University, Ames, 50011, IA, USA
[b] Center for Multiphase Flow Research and Education (CoMFRE), Iowa State University, Ames, 50011, IA, USA
[c] ANSYS Inc., 10 Cavendish Court, Lebanon, 03766, NH, USA
[d] Nanjing Tianfu Software Co.,Ltd., 11th floor, building B1, Jiulong Lake International Enterprise Park, Nanjing, Jiangsu 211100, PR China

ARTICLE INFO

MSC
0000
1111

Keywords:
Pseudo-turbulent heat flux
Gas-solid heat transfer
Computational fluid dynamics
Direct numerical simulation

ABSTRACT

Flow past disperse solid particles or bubbles induces fluctuations in carrier fluid velocity, which correlate with temperature fluctuations in non-isothermal flows resulting in the pseudo-turbulent heat flux (PTHF). In the Eulerian-Eulerian (EE) two-fluid (TF) model, the transport of PTHF is shown to be an important contributor to the overall energy budget, and is modeled using a pseudo-turbulent thermal diffusivity (PTTD). The PTHF and PTTD were originally quantified using particle-resolved direct numerical simulation (PR-DNS) data, and correlations were developed over a range of solid volume fraction ($0.1 \leq \epsilon_s \leq 0.5$) and mean slip Reynolds number ($1 \leq Re_m \leq 100$) for a Prandtl number of 0.7. However, the original PTTD correlation diverges to infinity as the solid volume fraction goes to zero, which is physically unrealistic. This singular behavior is problematic for EE TF simulations at particle material fronts where solid volume fraction values can fall below the lower limit of existing data ($\epsilon_s = 0.1$) to zero in the pure carrier phase. In this work, additional PR-DNS data are reported for $\epsilon_s < 0.1$, and improved correlations are developed for the PTHF and PTTD. The new PTTD correlation is non-singular, and both the PTHF and PTTD decay exponentially to zero as the solid volume fraction approaches zero, which is physically reasonable. This improves prediction of PTHF transport in dilute flow using EE TF heat transfer simulations.

1. Introduction

Gas-solid heat transfer plays a critical role in applications ranging from chemical looping combustion (Shen et al., 2008) to carbon-neutral energy generation (Abanades et al., 2004). Understanding gas-solid heat transfer is essential for design process and process optimization in unit operations. Such technological advances are key to limiting climate change and achieving carbon neutrality by 2050 (Shukla et al., 2019). Multiphase computational fluid dynamics (MCFD) has drawn the attention of researchers in the exploration of complex physical phenomena of gas-solid flow due to relatively low cost compared to experiments at scale (Papadikis et al., 2009; Boateng and Mtui, 2012; Xue et al., 2011). For MCFD simulations, the Eulerian-Eulerian (EE) two-fluid (TF) model in which the particulate and the fluid phases are considered to be interpenetrating continua (Drew, 1983) is widely used. Based on this assumption, the average flow variables in each phase are modeled as continua governed by conservation laws for phase-averaged quantities that can simultaneously occupy the same spatial location at the same time. The conservation equations contain coupling terms representing the interphase transfer of mass, momentum, and energy. In device-scale applications, the modeling of these coupling terms determines the predictive capability of multiphase CFD simulations.

Particle-resolved direct numerical simulation (PR-DNS) provides a model-free solution with complete three-dimensional time-dependent fields of velocity, pressure, and temperature of gas-solid heat transfer. Therefore, PR-DNS can be used to model the unclosed terms that appear in EE TF model (Tenneti and Subramaniam, 2014). The average interphase transfer of momentum and energy of the EE TF model has been investigated based on the velocity and temperature fields generated by PR-DNS (Mehrabadi et al., 2015, 2016; Sun et al., 2015, 2016).

Specifically, in the absence of mass transfer between phases, the governing equation of the fluid-phase heat transfer in the Eulerian-Eulerian two-fluid model (Syamlal et al., 1993; Garg, 2009) is

* Corresponding author.
E-mail addresses: Jiazhong@iastate.edu (J. Zhou), Bo.Sun@ansys.com (B. Sun), Shankar@iastate.edu (S. Subramaniam).

https://doi.org/10.1016/j.ces.2023.119371
Received 6 February 2023; Received in revised form 25 September 2023; Accepted 5 October 2023
Available online 11 October 2023

$$\underbrace{\frac{\partial}{\partial t}\{\rho_f \varepsilon_f c_{pf}\langle T^{(f)}\rangle\}}_{\text{unsteady term}} + \underbrace{\frac{\partial}{\partial x_j}\{\rho_f \varepsilon_f c_{pf}\langle u_j^{(f)}\rangle\langle T^{(f)}\rangle\}}_{\text{mean flow convection}} = \underbrace{\left\langle \frac{\partial I_f}{\partial x_j} q_j \right\rangle}_{\substack{\text{(1) average gas-solid} \\ \text{heat transfer}}} - \underbrace{\frac{\partial}{\partial x_j}\langle I_f q_j\rangle}_{\substack{\text{(2) average conduction} \\ \text{in the fluid phase}}} - \underbrace{\frac{\partial}{\partial x_j}\{\rho_f c_{pf}\langle I_f u_j''^{(f)} T''^{(f)}\rangle\}}_{\substack{\text{(3) pseudo-turbulent} \\ \text{heat flux term}}}, \quad (1)$$

where $\langle T^{(f)}\rangle$ is the average fluid-phase temperature, and it can be computed by averaging temperature field conditional on the presence of the fluid phase, such that

$$\langle T^{(f)}\rangle(\boldsymbol{x},t) = \frac{\langle I_f(\boldsymbol{x},t)T(\boldsymbol{x},t)\rangle}{\langle I_f(\boldsymbol{x},t)\rangle}, \quad (2)$$

where $I_f(\boldsymbol{x},t)$ is the fluid-phase indicator function that is unity if the point $\boldsymbol{x}$ lies on the fluid phase at time t, and zero otherwise, and the angle brackets denote ensemble-averaging of random fields over all particle configurations. In Eq. (1), ρ_f and c_{pf} are, respectively, the density and specific heat of the fluid phase, ε_f is the fluid volume fraction, q_j is the heat flux vector, $u_j''^{(f)} = u_j - \langle u_j^{(f)}\rangle$ and $T''^{(f)} = T - \langle T^{(f)}\rangle$ are, respectively, the velocity and temperature fluctuations.

The flux term $\langle I_f u_j''^{(f)} T''^{(f)}\rangle$ in the average fluid temperature equation (Eq. (1)) is called pseudo-turbulent heat flux (PTHF). In this unclosed term, the velocity fluctuation component $u_j''^{(f)}$ can arise from inherent turbulent flow, but it can also be generated in laminar flow by the interactions of wakes due to the presence of particles. The PTHF term represents the covariance of gas-phase velocity fluctuations and temperature, and its transport in two-fluid CFD simulations is usually neglected due to lack of information. Sun et al. (2016) quantified the PTHF based on particle-resolved direct numerical simulation (PR-DNS) of steady thermally fully-developed flow past homogeneous particle assemblies. Their analysis showed that the transport of PTHF is an important contributor to the overall energy budget, as expressed in the mean fluid temperature equation. The transport of PTHF in multiphase CFD can be modeled using a gradient-diffusion hypothesis by introducing a pseudo-turbulent thermal diffusivity (PTTD) $\alpha_{PT,jk}$, which is defined by the relation $\langle I_f u_j''^{(f)} T''^{(f)}\rangle = -\alpha_{PT,jk}\partial\langle T^{(f)}\rangle/\partial x_k$. Sun et al. (2016) characterized the PTTD over the same range of solid volume fraction ($0.1 \le \varepsilon_s \le 0.5$) and mean slip Reynolds number ($1 \le Re_m \le 100$), and developed a correlation for the PTTD as a function of solid volume fraction and mean slip Reynolds number. Peng et al. (2019) incorporated this transport model for the PTTD and showed its importance in multiphase CFD simulations.

Although the PTHF has been investigated as summarized, one problem that is encountered in multiphase CFD, which typically involves inhomogeneous solid volume fraction fields, is the behavior of PTHF and PTTD at the edge of particle material fronts where the solid volume fraction goes to zero in the pure fluid region. Such particle material fronts are encountered at the top of the freeboard in a fluidized bed. Sun's correlation for PTTD predicts an infinite value as the solid volume fraction goes to zero, which is unphysical and leads to instabilities in the numerical solution of the multiphase CFD equations. Therefore, in this work we examine the behavior of PTHF and PTTD at very low volume fractions to definitively address their behavior in this limit. We also propose improved PTHF and PTTD correlations that are accurate at low solid volume fraction, resulting in stable MCFD simulations. This article is structured as follows. Section 2 introduces the PR-DNS method for flow past a fixed particle assembly that is used for quantifying PTHF and PTTD. Section 3 provides quantitative analysis of the PTHF at lower volume fractions and proposes the improved PTHF and PTTD correlations. Section 4 summarizes the principal findings of this work.

2. Problem formulation

The heat transfer problem formulation in this study is identical to that described in Sun et al. (2016) for steady flow past a homogeneous assembly of monodisperse spherical particles. We briefly summarize the problem formulation, governing equations, and PR-DNS setup in this section.

We have previously argued (Tenneti et al., 2013) that in order to specify closure models for the unclosed terms it is natural to simulate a statistically homogeneous gas–solid suspension using PR-DNS. The closure for the average interphase momentum transfer or 'drag law' in the hydrodynamic problem has been inferred from PR-DNS of steady flow past statistically homogeneous particle suspensions driven by a constant mean pressure gradient in periodic domains. This problem setup ensures that the flow field is statistically homogeneous such that the mean velocity is a constant that does not vary in space, and although the mean pressure varies linearly in the flow direction, the fluctuating pressure is periodic. Statistics such as the average interphase momentum transfer can be easily obtained by volume averaging.

In the heat transfer problem, the effect of continuous heating (or cooling) of the fluid by the particles along the flow direction causes the average fluid temperature to vary in that direction. Although the hydrodynamic problem is statistically homogeneous, anisotropy in the mean fluid velocity results in a statistically inhomogeneous average fluid temperature field. Fig. 1a shows the contours of non-dimensional fluid temperature (defined by Eq. (8)) in steady flow through a cubic domain due to a constant imposed mean pressure gradient in the streamwise direction, revealing how the fluid is cooled by the particles. Fig. 1b shows that the average non-dimensional fluid temperature (defined by Eq. (14)) monotonically decreases in the streamwise direction because the fluid that is hotter than the particles at the inlet is progressively cooled as it flows over the particles and loses heat to them. Although the hydrodynamic problem is statistically homogeneous, the average fluid temperature field is statistically inhomogeneous. Statistics such as the average Nusselt number cannot be obtained by volume averaging, but vary in the streamwise coordinate and are subject to greater statistical variability. Therefore, PR-DNS methodologies that are used to specify a closure model for the average Nusselt number in terms of the average solid volume fraction and mean slip Reynolds number must account for this inhomogeneity in the fluid temperature field.

One approach is to solve the heat transfer problem with an inflow boundary condition on the inlet side and an outflow boundary condition on the outlet side (Tavassoli et al., 2013). This results in a thermally developing flow right next to the inlet plane in which the average Nusselt number varies with axial distance, eventually transitioning to a thermally fully developed flow where the average Nusselt number becomes independent of axial location. In this setup, averaging should only be performed in the thermally fully-developed region of the flow domain when computing statistics such as the average Nusselt number. This reduces the available region in the solution domain to obtain desired heat transfer statistics and it also introduces uncertainties in the definition of the thermally fully developed region.

In order to circumvent these problems, we adopt the PR-DNS methodology of Tenneti et al. (2013) to study heat transfer in statistically homogeneous gas–solid flow in periodic domains, while still accounting for spatial inhomogeneity in the average fluid temperature and using the entire thermally fully developed flow domain to extract desired statistics. Following Tenneti et al. (2013) we use the analogy of thermally fully developed flow in a fixed bed of particles (in an average sense) with thermally fully developed flow in internal pipes to develop a thermal self-similarity condition that guarantees a statistically homogeneous Nusselt number (Tenneti et al., 2013). For internal pipe flow with isothermal walls held at T_w, the flow is said to be thermally fully developed when the scaled temperature $\frac{T(\boldsymbol{x},t) - T_w}{T_m(x) - T_w}$, which is the ratio of the driving force (temperature difference) in the numerator to the response in the denominator (heat flux is written as a heat transfer coefficient times this temperature difference), does not change with the streamwise coordinate x. Here T_m is the bulk or 'mixing cup' temperature that is defined in particle-laden flows for each particle configuration ω by

$$T_m(x,t;\omega) = \frac{\int_{A_f} (\boldsymbol{u}T)\cdot \boldsymbol{e}_1 dA_f}{\int_{A_f} \boldsymbol{u}\cdot \boldsymbol{e}_1 dA_f}, \tag{3}$$

where $\boldsymbol{e}_1$ is the unit vector along the streamwise direction, and A_f is the cross-sectional area occupied by the fluid perpendicular to the streamwise direction.

Tenneti et al. (2013) and Sun et al. (2015) developed a thermal self-similarity condition in terms of a locally scaled fluid temperature field $\theta(\boldsymbol{x},t)$ defined as

$$\theta(\boldsymbol{x},t) = \frac{T(\boldsymbol{x},t) - T_s}{\langle T_m\rangle(x) - T_s}, \tag{4}$$

where T_s is the constant temperature of the isothermal particles, and $\langle T_m\rangle(x)$ is the average bulk fluid temperature at a streamwise location x, defined by

$$\langle T_m\rangle(x,t) \equiv \int_{\omega\in\Omega} T_m(x,t;\omega) dP_\omega, \tag{5}$$

where ω represents a particle configuration which occurs with probability dP_ω. Clearly $\langle T_m\rangle - T_s$ in Eq. (4) is analogous to $T_m - T_w$ in the definition of scaled temperature for internal pipe flow, and it is in this sense that thermally fully developed particle-laden flow is analogous (in an average sense) to internal pipe flow. This thermal self-similarity condition requires that

$$\frac{\partial\theta}{\partial x} = \frac{\partial}{\partial x}\left(\frac{T(\boldsymbol{x},t) - T_s}{\langle T_m(x,t)\rangle - T_s}\right) = 0 \tag{6}$$

for the flow to be thermally fully developed. Just as in thermally fully developed pipe flow, this condition guarantees that at steady state the ratio of the driving force (temperature difference) in the numerator to the response (heat flux) in the denominator does not change with the flow coordinate x.

2.1. Governing equations

The assumptions made in this heat transfer problem are: (i) isothermal particles (see Appendix A) with a single spatially uniform temperature for all particles that is constant in time, (ii) negligible free convection (see Appendix B), and (iii) neglect of radiation and viscous heating. In the absence of viscous heating, radiation, and free convection effects, the governing equation for the fluid temperature field $T(\boldsymbol{x},t)$ is

$$\frac{\partial T}{\partial t} + \frac{\partial(u_j T)}{\partial x_j} = \alpha_f \frac{\partial^2 T}{\partial x_j \partial x_j}, \tag{7}$$

where $\alpha_f = k_f/\rho_f c_{pf}$ is the thermal diffusivity in the fluid phase, and k_f is the thermal conductivity in the fluid phase. The Dirichlet boundary condition $T = T_s$ is applied at the surface of each particle corresponding to isothermal particles.

Since the boundary conditions at the domain boundaries are in terms of θ, it would appear to be easier to rewrite Eq. (7) in terms of θ and solve directly for θ. However, the evolution equation for θ contains additional terms that represent the evolution of the bulk temperature T_m. Therefore, in order to solve for θ we need to solve an additional equation for T_m. Moreover, solving for the evolution equation for T_m requires the computation of heat flux from every particle that intersects the plane perpendicular to the mean flow at each x location in the direction of the mean flow. Since there is a finite number of particles in the computational domain, the solution may suffer from statistical error. Therefore, it turns out to be easier to transform the periodic boundary conditions on θ to obtain similarity conditions on the temperature field $T(\boldsymbol{x},t)$ and solve Eq. (7) for $T(\boldsymbol{x},t)$. In order to simplify the thermal similarity conditions, and also to homogenize the boundary conditions

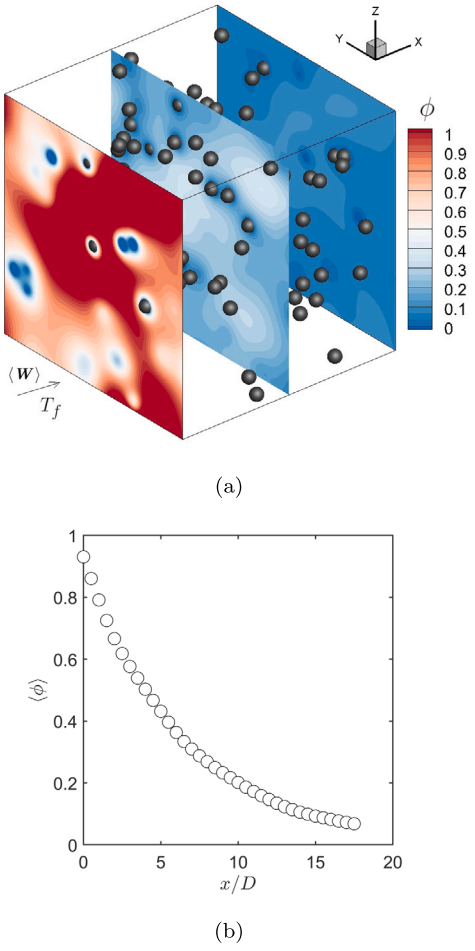

Fig. 1. (a) Contour of the non-dimensional fluid temperature field (see Eq. (8)) in flow past a fixed particle assembly. (b) The corresponding average non-dimensional fluid temperature along the axial location. $\langle \boldsymbol{W}\rangle$ is the mean slip velocity between the solid and fluid phase, T_f is the fluid temperature, and $\langle\phi\rangle$ is the average non-dimensional fluid temperature (see Eqs. (2) and (8)).

on the particle surfaces, we define a non-dimensional temperature field $\phi(\boldsymbol{x},t)$ as follows:

$$\phi(\boldsymbol{x},t) = \frac{T(\boldsymbol{x},t) - T_s}{\langle T_{m,in}\rangle - T_s}, \tag{8}$$

where $\langle T_{m,in}\rangle$ is the average bulk fluid temperature $\langle T_m\rangle(x)$ evaluated at $x = 0$.

The governing equation for the non-dimensional fluid temperature field $\phi(\boldsymbol{x},t)$ can be derived as

$$\frac{\partial\phi}{\partial t} + \frac{\partial(u_j\phi)}{\partial x_j} = \alpha_f \frac{\partial^2\phi}{\partial x_j \partial x_j}. \tag{9}$$

The isothermal boundary conditions on the particle surface reduce to $\phi = 0$, and the thermal similarity conditions now appear in a very simple form as

$$\phi(0,y,z) = r_h\phi(L,y,z) \tag{10a}$$

$$\phi(x,0,z) = \phi(x,L,z) \tag{10b}$$

$$\phi(x,y,0) = \phi(x,y,L) \tag{10c}$$

where r_h is the heat ratio defined by

$$r_h = \frac{\langle T_{m,in}\rangle - T_s}{\langle T_{m,out}\rangle - T_s}, \tag{11}$$

where $\langle T_{m,out} \rangle$ is the average bulk fluid temperature evaluated at $x = L$, and L is the length of the computational domain in the streamwise direction.

2.2. Computation of PTHF

Certain simplifications arise in computing the scaled PTHF $\langle I_f u_i''^{(f)} \phi''^{(f)} \rangle$ (where the non-dimensional fluid temperature fluctuation is defined as $\phi''^{(f)} = \phi - \langle \phi^{(f)} \rangle$) from the thermally fully developed solution that results from the thermal self-similarity condition imposed in periodic domains as described above. The non-dimensional fluid temperature field $\phi(\boldsymbol{x}, t)$ in Eq. (8) can be written as the product of the scaled non-dimensional fluid temperature and the average non-dimensional bulk fluid temperature $\langle \phi_m \rangle(x, t)$:

$$\begin{aligned} \phi(\boldsymbol{x}, t) &= \left(\frac{T(\boldsymbol{x}, t) - T_s}{\langle T_m \rangle(x, t) - T_s} \right) \left(\frac{\langle T_m \rangle(x, t) - T_s}{\langle T_{m,in} \rangle - T_s} \right) \\ &= \theta(\boldsymbol{x}, t) \langle \phi_m \rangle(x, t). \end{aligned} \tag{12}$$

Multiplying the above equation by the fluid indicator function I_f, taking the expectation based on the definition in Eq. (2) leads to the corresponding relation

$$\langle \phi^{(f)} \rangle(\boldsymbol{x}, t) = \langle \theta^{(f)} \rangle(\boldsymbol{x}, t) \langle \phi_m \rangle(x, t). \tag{13}$$

Since the scaled temperature field θ is statistically homogeneous, the above equation can be further simplified as

$$\langle \phi^{(f)} \rangle(\boldsymbol{x}, t) = \langle \theta^{(f)} \rangle(t) \langle \phi_m \rangle(x, t), \tag{14}$$

revealing that all spatial inhomogeneity in $\langle \phi^{(f)} \rangle$ arises purely from $\langle \phi_m \rangle$. This observation leads to simplifications in computing the scaled PTHF.

We now deduce the PTHF in terms of the scaled fluid temperature $\theta(\boldsymbol{x}, t)$ that is statistically homogeneous. Substituting the definition of the non-dimensional fluid temperature fluctuations $\phi''^{(f)}(\boldsymbol{x}) = \phi(\boldsymbol{x}) - \langle \phi^{(f)} \rangle(x)$ into the expression for the ensemble-averaged PTHF $\langle I_f u_i''^{(f)} \phi''^{(f)} \rangle(x)$ and using the relation $\phi = \theta \langle \phi_m \rangle$ (see Eq. (12)), leads to the following expression

$$R_{i\phi}^{(f)} \equiv \langle I_f u_i''^{(f)} \phi''^{(f)} \rangle(x) = \langle I_f u_i''^{(f)} \theta \rangle \langle \phi_m \rangle(x) = R_{i\theta}^{(f)} \langle \phi_m \rangle(x), \tag{15}$$

where $R_{i\theta}^{(f)} \equiv \langle I_f u_i''^{(f)} \theta \rangle$. Note that although $\langle I_f u_i''^{(f)} \phi''^{(f)} \rangle$ is inhomogeneous in x, the covariance of velocity and scaled temperature $R_{i\theta}^{(f)}$ is expected to be statistically homogeneous since both the fluid velocity field u_i and the scaled fluid temperature field θ are statistically homogeneous. Again, all spatial inhomogeneity in the scaled PTHF arises purely from $\langle \phi_m \rangle$. In a previous study (Sun et al., 2016) showed that the average non-dimensional bulk fluid temperature $\langle \phi_m \rangle(x)$ decays exponentially with axial distance.

2.3. PR-DNS method

The PR-DNS approach in this study is identical to that described in Sun et al. (2016) for steady flow past a homogeneous assembly of monodisperse spherical particles. The particles are maintained at a constant temperature and distributed in a random configuration over a cubic domain with periodic boundary conditions to produce a predefined solid volume fraction. In this work, the solid volume fraction is extended to low values and each case is simulated at three different Reynolds numbers. Table 1 summarizes the relevant simulation parameters for generating the PR-DNS data in this study.

A couple of details regarding the implementation of the governing equations (Eq. (9)) along with its boundary conditions (Eqs. (10)) and Eq. (11) are noteworthy. When solving Eq. (9), the fluid velocity field is taken to be a given quantity that is obtained from the hydrodynamic solution for that particle configuration. In this formulation, because of the isothermal boundary condition on particles, the fluid velocity field does not need to be evolved in time and is maintained the same while the temperature field evolves to a steady state. The average bulk temperature at the inlet appears in the definition of ϕ (see Eq. (8)), and the average bulk temperature at a given axial location x appears in the definition of $\theta(x)$. Although mathematically the average bulk temperature is defined by Eq. (5), in practice the average bulk temperature is computed separately for each realization as a cross-sectional average (see Eq. (3)). If the ensemble-average were used then multiple independent simulations would need to be performed in parallel, and the ensemble–averaged bulk temperature at the inlet would have to be computed at every time step. The same procedure would be needed when post-processing statistics related to θ (Eq. (4)). However, in practice θ is also computed using the same cross-sectionally averaged T_m for that realization.

Table 1
Parameters for heat transfer simulation in steady flow past random fixed assemblies of particles. The physical parameters are the solid volume fraction ϵ_s and the mean slip Reynolds number Re_m. The numerical parameters are the ratio of the box length to the particle diameter L/D and the grid resolution $D_m = D/\Delta x$. The number of particles N_p is determined by ϵ_s and L. Five independent simulations of each case are simulated to reduce statistical variability.

ϵ_s	Re_m	L/D	N_p	D_m
0.01	1,50,100	18	111	20
0.03	1,50,100	15	193	20
0.05	1,50,100	12	165	20
0.1	1,50,100	7.5	80	20
0.2	1,50,100	7.5	161	20
0.3	1,50,100	5	71	30
0.4	1,50,100	5	95	30
0.5	1,50,100	4	61	40

In the following, we first quantify $\langle I_f u_i''^{(f)} \theta \rangle$ and then propose an improved PTHF correlation for it in Sec. 3.1. In Sec. 3.2 we modify the exponentially decaying coefficient for the average bulk fluid temperature model that is later used in the gradient-diffusion model for the PTHF. In Sec. 3.3 we propose a modification to the PTTD correlation in which the modified PTHF correlation and the modified decay coefficient appear. In Sec. 3.4, a scale analysis is conducted to validate the scale separation assumption for local closure model development in statistically homogeneous gas-solid flow.

3. Results and discussion

3.1. Quantifying and modeling the PTHF

In order to quantify the PTHF term, we first solve Eq. (9) by using the PR-DNS approach to extract the non-dimensional fluid temperature field $\phi(\boldsymbol{x}, t)$ and the average non-dimensional bulk fluid temperature $\langle \phi_m \rangle(x, t)$. By using the relation $\phi = \theta \langle \phi_m \rangle$ (see Eq. (12)), we can compute the non-dimensional scaled fluid temperature field $\theta(\boldsymbol{x}, t)$ for quantifying the statistical homogeneous $\langle I_f u_i''^{(f)} \theta \rangle$.

It is of interest to examine the covariance of velocity and scaled temperature in an orthogonal coordinate system aligned with the mean velocity vector. Our observations indicate that the component of fluctuating velocity aligned with the mean flow direction shows strong correlation with the scaled temperature (see Fig. 2a), while the fluctuating velocity components perpendicular to the mean flow exhibit weak correlation with the scaled temperature (see Figs. 2b and 2c). The joint probability distribution function (PDF) of the velocity and scaled temperature is presented in Fig. 2d, showing that the PDFs of $I_f u_y''^{(f)} \theta$ and $I_f u_z''^{(f)} \theta$ are almost identical to a zero-mean Gaussian distribution. As a result, the PTHF in the cross-stream directions $\langle I_f u_\perp''^{(f)} \theta \rangle$ are negligible, while the streamwise component of the PTHF $\langle I_f u_\parallel''^{(f)} \theta \rangle$ is the dominant and non-negligible contribution to the flux. This observation is consistent with the characteristics of the pseudo-turbulent Reynolds stress tensor, defined as $\langle I_f u_i''^{(f)} u_j''^{(f)} \rangle / \langle I_f \rangle$, where the cross-correlation

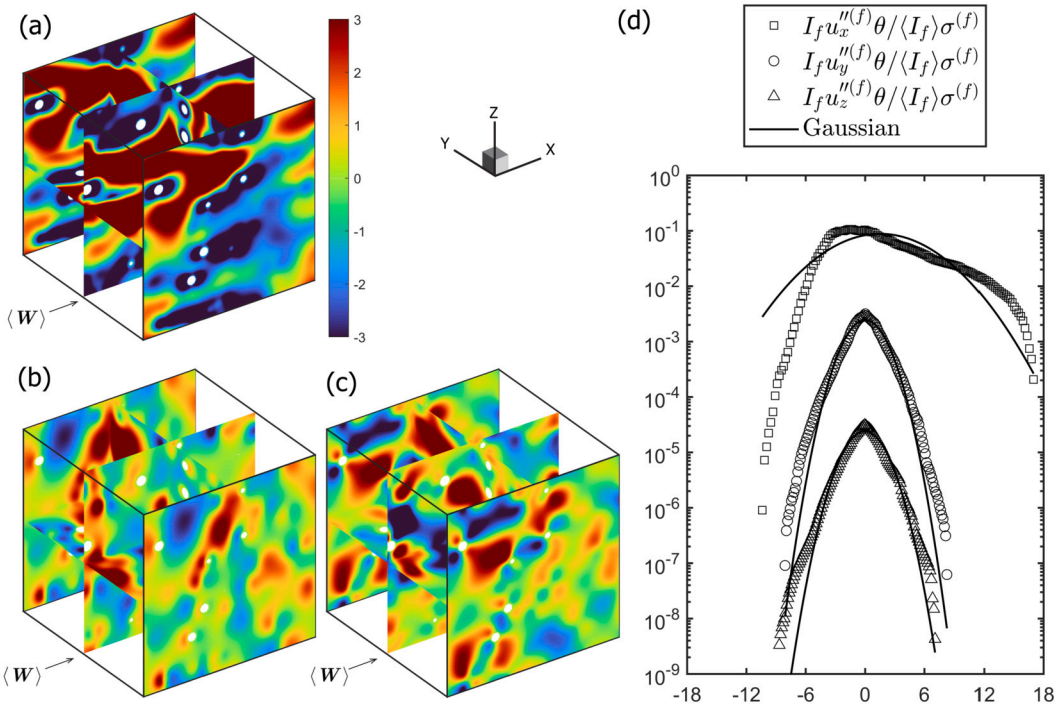

Fig. 2. Covariance of fluctuating velocity and scaled temperature obtained from PR-DNS data at $\varepsilon_s = 0.01$ and $Re_m = 1$ normalized by $\sigma^{(f)} = (2k_f/3)^{1/2}(\langle I_f\theta''\theta''\rangle/\langle I_f\rangle)^{1/2}$, where k_f represents the kinetic energy in fluid-phase velocity fluctuations and $\theta'' = \theta - \langle\theta^{(f)}\rangle$ is the scaled temperature fluctuation. The mean flow velocity is in the positive x direction and the mean temperature gradient is aligned with the mean flow. The left panel displays contours of $I_f u_i''^{(f)}\theta/\langle I_f\rangle\sigma^{(f)}$: (a) $I_f u_x''^{(f)}\theta/\langle I_f\rangle\sigma^{(f)}$, (b) $I_f u_y''^{(f)}\theta/\langle I_f\rangle\sigma^{(f)}$, and (c) $I_f u_z''^{(f)}\theta/\langle I_f\rangle\sigma^{(f)}$. The right panel (d) shows the joint probability distribution function (PDF) of the velocity and scaled temperature. Note that the mean value of the joint PDF represents the covariance in the PTHF. Each PDF has been shifted up by two decades with respect to the lower one. Associating $\parallel$ with x and $\perp_1$ and $\perp_2$ with y and z, respectively, we see that $\langle I_f u_\parallel''^{(f)}\theta\rangle$ is dominant and nonzero whereas the other components are negligible.

between the streamwise and cross-stream velocity fluctuations is negligible $\langle I_f u_\parallel''^{(f)} u_\perp''^{(f)}\rangle \approx 0$ (see Mehrabadi et al., 2015.) These findings hold when the mean temperature gradient is not imposed but is established along the mean flow direction because of cooling (or heating) of fluid by the particles, as is the case in this PTHF study. For this setup we found that only the streamwise component of the PTHF $\langle I_f u_\parallel''^{(f)}\theta\rangle$ is non-negligible. However, it should be noted that when the mean flow direction and the mean fluid temperature gradient are not aligned, the PTHF may have non-negligible contributions in other components as well.

We quantify the magnitude of PTHF over a cross-sectional plane at a given axial location over M realizations as

$$\langle I_f u_\parallel''^{(f)}\theta\rangle(x) \approx \frac{1}{M}\sum_{\omega=1}^{M}\left\{\frac{1}{A}\int_0^A \{I_f u_\parallel''^{(f)}\theta\}(\boldsymbol{x};\omega)dA\right\}, \tag{16}$$

where A is the cross-section area that is located at x and $u_\parallel''^{(f)}$ is the component of fluctuating fluid velocity in the streamwise direction. Fig. 3 illustrates the ensemble-averaged cross-sectional PTHF obtained from the PR-DNS simulations of heat transfer in steady flow past random fixed assemblies of particles in the volume fraction range $0.01 \le \varepsilon_s \le 0.03$ at $Re_m = 100$. This result also confirms that the statistical homogeneity in the ensemble-averaging of PTHF can be achieved by using five realizations ($m = 5$) as suggested in the previous study. Next, we compute $\langle I_f u_\parallel''^{(f)}\theta\rangle$ by using a volume average as

$$\langle I_f u_\parallel''^{(f)}\theta\rangle = \frac{1}{L}\int_0^L \langle I_f u_\parallel''^{(f)}\theta\rangle(x)dx, \tag{17}$$

and this quantity only depends on the average solid volume fraction and mean slip Reynolds number.

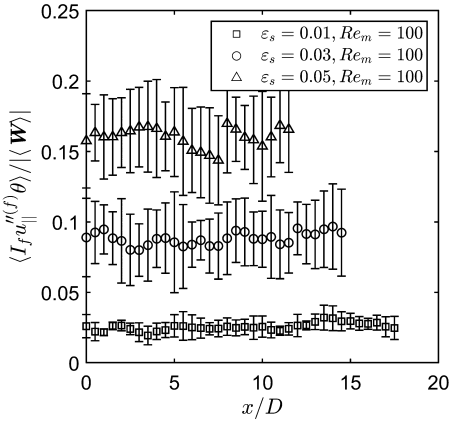

Fig. 3. Variation of the ensemble-averaged PTHF normalized by the magnitude of mean slip velocity $|\langle \boldsymbol{W}\rangle|$ along axial location x over 5 MIS in the range $0.01 \le \varepsilon_s \le 0.03$ at $Re_m = 100$. The error bars indicate 95% confidence intervals.

The quantified PTHF term as a function of solid volume fraction and Reynolds number is shown as circles in Fig. 4. The original PTHF data set ($0.1 \le \varepsilon_s \le 0.5$) is shown as black circles while the PTHF data from this work is shown as red circles. The original PTHF correlation is given by

$$\langle I_f u_\parallel''^{(f)}\theta\rangle = (1-\varepsilon_s)(0.2 + 1.2\varepsilon_s - 1.24\varepsilon_s^2)\exp(-0.002 Re_m)|\langle \boldsymbol{W}\rangle|, \tag{18}$$

which predicts the PTHF over the range of solid volume fraction ($0.1 \le \varepsilon_s \le 0.5$) and mean slip Reynolds number ($1 \le Re_m \le 100$) for Prandtl number of 0.7, where $|\langle \boldsymbol{W}\rangle|$ is the mean slip velocity.

Fig. 4 shows how the PTHF term varies with respect to the solid volume fraction and mean slip Reynolds number. At higher solid vol-

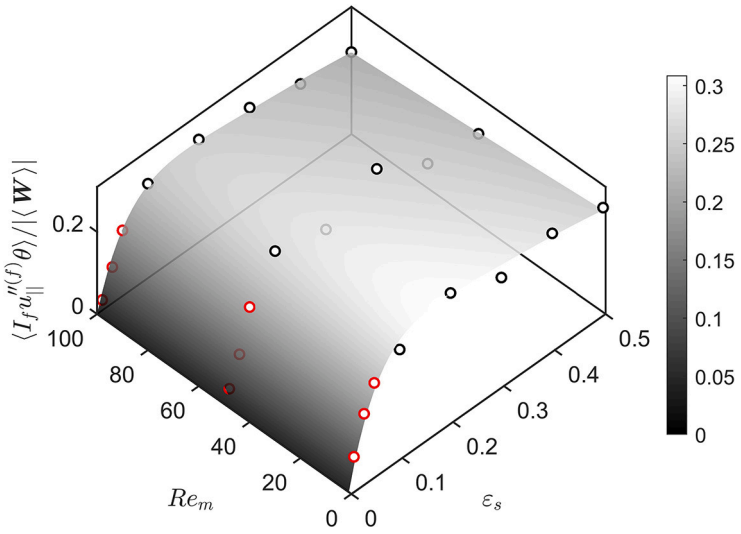

Fig. 4. Least squares fit of PTHF numerical results for the proposed PTHF correlation. Circle represent the volume-averaged $\langle I_f u_{\|}''^{(f)}\theta\rangle$ results using Eqs. (16) and (17) over 5 PR-DNS data. Red is PTHF for the range $0.01 \le \varepsilon_s \le 0.03$ and $1 \le Re_m \le 100$, which is obtained from this study while black circles originated from a previous study.

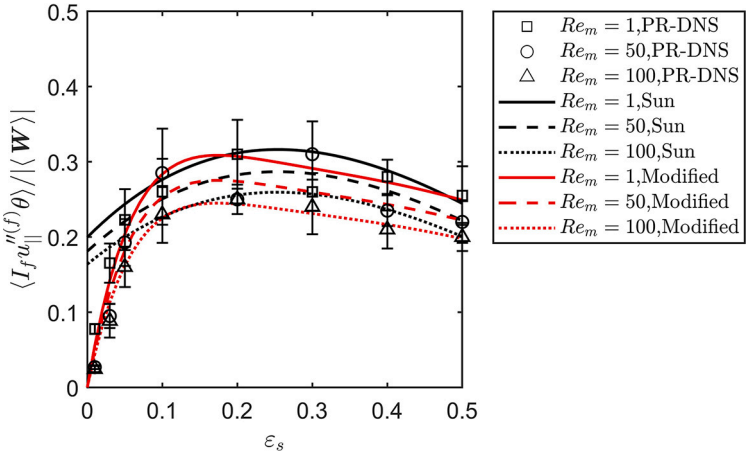

Fig. 5. Comparison of the pseudo-turbulent heat flux (PTHF) in the range $0 \le \varepsilon_s \le 0.5$ and $1 \le Re_m \le 100$: symbols represent the PTHF obtained from PR-DNS data; black (original) and red (modified) lines represent the PTHF correlation. Error bars represent 95% confidence intervals using 5 MIS.

ume fraction ($\varepsilon_s > 0.1$), the PTHF term is relatively constant, while at lower solid volume fraction ($\varepsilon_s < 0.1$), the PTHF exponentially decays to zero as solid volume fraction goes to zero ($\varepsilon_s \to 0$). However, its variation with Reynolds number is relatively small compared to solid volume fraction. Consequently, the modified PTHF correlation should capture those trends. Inspired by the original PTHF correlation, our new correlation is proposed as

$$\langle I_f u_{\|}''^{(f)}\theta\rangle = \{(1-\varepsilon_s)(c_1\varepsilon_s + c_2\varepsilon_s^2 + c_3\varepsilon_s^3) + [1-\exp(c_4\varepsilon_s)]\}\exp(c_5 Re_m)|\langle \boldsymbol{W}\rangle|, \tag{19}$$

with the following constants,

$$c_1 = -5.11, \quad c_2 = 10.10, \quad c_3 = -10.85, \quad c_4 = -10.96, \quad c_5 = -0.002089.$$

The above coefficients are computed based on a least-squares fit with the PTHF results obtained from the PR-DNS simulations (Fig. 4). The mathematical form of the new correlation is similar to those of the previous but with a few exceptions. There is a constant term in the polynomial of the original PTHF (Eq. (18)), contributing to the non-zero limit of PTHF when particles no longer exist ($\varepsilon_s = 0$), which is inconsistent with the flow physics and PR-DNS data extracted at low ε_s. In practice, this may cause problems when using the PTHF model at the edge of particle material fronts where the solid volume fraction is nearly zero in the pure fluid region. The PTHF term should be zero at $\varepsilon_s = 0$ in such applications. Based on this expectation, the form of the new correlation is constructed so that it is zero when the solid volume fraction equals zero. Another difference is that we include an exponential function, accompanied by the high-order polynomial, to capture the exponential decay trend when the solid volume fraction approaches zero. Therefore, the new PTHF correlation, modified from the original counterpart, can be viewed as a combination of a polynomial that is dominant in dense flow regions with an exponential decay function that is responsible for capturing the physical behavior of PTHF in dilute flow (e.g., gas-solid flows at the top of the freeboard in a fluidized bed). In Fig. 5, the black and red lines illustrate the behavior of the original and modified PTHF correlations, respectively, as a function of solid volume fraction and mean slip Reynolds number.

3.2. Decay coefficient modification

In Eq. (1), the transport of PTHF term needs to be modeled in CFD simulations based on the two-fluid model. A gradient-diffusion model, similar to the turbulent scalar flux models in single-phase flow (Fox, 2003), has been proposed and validated by Sun et al. (2016). The gradient-diffusion model is:

$$\frac{\langle I_f u_i''^{(f)} \phi''^{(f)} \rangle}{\langle I_f \rangle} = -\alpha_{PT,ij} \frac{\partial \langle \phi^{(f)} \rangle}{\partial x_j}, \tag{20}$$

where $\alpha_{PT,ij}$ is the pseudo-turbulent thermal diffusivity (PTTD). In general, $\alpha_{PT,ij}$ should be a second-order, anisotropic tensor characterizing the transport of PTHF in different directions not necessarily aligned with the gradient of phase-averaged mean fluid temperature.

Mehrabadi et al. (2015) quantified the pseudo-turbulent Reynolds stress (PTRS) tensor $R_{ij}^{(f)} = \langle I_f u_i''^{(f)} u_j''^{(f)} \rangle / \langle I_f \rangle$ in steady flow past fixed assemblies of spheres using PR-DNS simulation. The anisotropy of the PTRS tensor was computed over a range of solid volume fraction and mean slip Reynolds number. It was found that the PTRS tensor exhibits two independent diagonal components, $R_{\parallel,\parallel}^{(f)}$ and $R_{\perp,\perp}^{(f)}$, that characterize the PTRS parallel and perpendicular to the mean flow direction, respectively. The cross-correlation between the streamwise and cross-stream velocity fluctuations was found to be negligible $\langle I_f u_\parallel''^{(f)} u_\perp''^{(f)} \rangle \approx 0$. Hence, the PTRS is orthotropic corresponding to two-component axisymmetric turbulence (Pope, 2000). Those PR-DNS simulations also revealed that the PTRS component in the parallel direction $R_{\parallel,\parallel}^{(f)}$ is dominant compared to the perpendicular direction $R_{\perp,\perp}^{(f)}$. This lends support to our findings that the streamwise component of the PTHF is non-zero whereas the other components are negligible in this setup.

In the general case where the mean temperature gradient is imposed at an arbitrary angle to the mean flow direction, it will have non-zero components in the cross-stream directions also. Generalizing the gradient-diffusion assumption by introducing a pseudo-turbulent thermal diffusivity (PTTD) tensor results in the following model:

$$R_{i\phi}^{(f)} = \alpha_{PT,ij} \frac{\partial \langle \phi^{(f)} \rangle}{\partial x_j} \tag{21}$$

where the pseudo-turbulent thermal diffusivity (PTTD) $\alpha_{PT,ij}$ is a second-order tensor. The subscript 'PT' will be omitted in the index notation in the tensor components for simplicity. Rewriting this relation in terms of the parallel and perpendicular components and expanding each component, we have

$$R_{\parallel\phi}^{(f)} = \alpha_{\parallel,\parallel} \frac{\partial \langle \phi^{(f)} \rangle}{\partial x_\parallel} + \alpha_{\parallel,\perp_1} \frac{\partial \langle \phi^{(f)} \rangle}{\partial x_{\perp_1}} + \alpha_{\parallel,\perp_2} \frac{\partial \langle \phi^{(f)} \rangle}{\partial x_{\perp_2}} \tag{22}$$

$$R_{\perp_1\phi}^{(f)} = \alpha_{\perp_1,\parallel} \frac{\partial \langle \phi^{(f)} \rangle}{\partial x_\parallel} + \alpha_{\perp_1,\perp_1} \frac{\partial \langle \phi^{(f)} \rangle}{\partial x_{\perp_1}} + \alpha_{\perp_1,\perp_2} \frac{\partial \langle \phi^{(f)} \rangle}{\partial x_{\perp_2}} \tag{23}$$

$$R_{\perp_2\phi}^{(f)} = \alpha_{\perp_2,\parallel} \frac{\partial \langle \phi^{(f)} \rangle}{\partial x_\parallel} + \alpha_{\perp_2,\perp_1} \frac{\partial \langle \phi^{(f)} \rangle}{\partial x_{\perp_1}} + \alpha_{\perp_2,\perp_2} \frac{\partial \langle \phi^{(f)} \rangle}{\partial x_{\perp_2}} \tag{24}$$

This is a under-determined problem for the general case because we have only three equations but nine unknown components of the PTTD tensor (it is not clear that the physics of pseudo-turbulence dictate that symmetry relations should be applicable for the PTTD in general).

In our current collinear setup with the mean temperature gradient aligned with the mean slip velocity, statistical symmetry implies that only one of the cross-stream components is independent, thereby reducing the number of unknown PTTD components to four: $\alpha_{\parallel,\parallel}$, $\alpha_{\parallel,\perp}$, $\alpha_{\perp,\parallel}$, and $\alpha_{\perp,\perp}$. With a mean temperature gradient that has only a nonzero streamwise component, we can infer $\alpha_{\parallel,\parallel}$ from the first equation, and the remaining equations tell us that $\alpha_{\perp_1,\parallel}$ and $\alpha_{\perp_2,\parallel}$ are zero because the mean gradient does not induce PTHF components in the cross-stream directions (cf. Figs. 2b and 2c.). Assuming symmetry of $\alpha_{\parallel,\perp}$ and $\alpha_{\perp,\parallel}$ leaves only one component $\alpha_{\perp,\perp}$ undetermined in this case. Peng et al. (2019) assumed that the orthotropic nature of the PTRS is preserved in the PTTD to determine the $\alpha_{\perp,\perp}$ component by:

$$\alpha_{\perp,\perp} = \left(\frac{R_{\perp,\perp}^{(f)}}{R_{\parallel,\parallel}^{(f)}} \right) \alpha_{\parallel,\parallel}. \tag{25}$$

The findings of this paper do not contradict the assumption of Peng et al. (2019), but neither do they provide validation for it.

PR-DNS simulations of gas-solid heat transfer where there is a nonzero angle between the mean flow and the gradient of the mean fluid temperature are required to test this assumption. In such cases, the cross-stream PTHF will depend on the angle between the mean flow and the mean fluid temperature gradient. A comprehensive examination of the anisotropic transport of the PTHF would require an inhomogeneous PR-DNS set-up where there is transport of PTHF in different directions from that of the mean fluid temperature gradient. Such an investigation is beyond the scope of this paper. In this study, the PR-DNS set-up allows only the gradient of the mean fluid temperature in the streamwise direction to be non-zero. Therefore, we only quantify the axial component of the PTHF, which is aligned with the gradient of the mean fluid temperature. As a result, the pseudo-turbulent thermal diffusivity tensor reduces to a scalar α_{PT} that represents the transport of PTHF parallel to the mean flow direction. Hence, the gradient-diffusion model along the streamwise direction is:

$$\frac{\langle I_f u_\parallel''^{(f)} \phi''^{(f)} \rangle(x)}{\langle I_f \rangle} = -\alpha_{PT} \frac{\partial \langle \phi^{(f)} \rangle}{\partial x}. \tag{26}$$

The above definition states that the magnitude of the PTHF is proportional to the spatial gradient of the average non-dimensional fluid temperature $\langle \phi^{(f)} \rangle$. In thermally fully developed gas-solid flow, the average bulk fluid temperature shows an exponential decay with respect to axial distance, which is similar to internal forced heat convection in a pipe problem. It should be noted that the average fluid temperature field $\langle \phi^{(f)} \rangle$ defined in Eq. (14) is a product of the scaled temperature field θ and the average bulk fluid temperature $\langle \phi_m \rangle(x)$, and obeys the form

$$\langle \phi_m \rangle(x) = e^{-\lambda_m x / D}, \tag{27}$$

where λ_m is the non-dimensional decay coefficient. Sun et al. (2016) proposed a decay coefficient of the form

$$\lambda_m = \frac{6\pi\varepsilon_s \langle Nu \rangle}{4(Re_m + 1.4)Pr}. \tag{28}$$

Consequently, a mathematical model for the pseudo-turbulent thermal diffusivity α_{PT} can then be derived by substituting Eqs. (14), (15), and (27) into Eq. (26) to obtain

$$\alpha_{PT} = \frac{D}{\lambda_m} \frac{\langle I_f u_\parallel''^{(f)} \theta \rangle}{(1-\varepsilon_s)\langle \theta^{(f)} \rangle}. \tag{29}$$

Fig. 6 compares the mathematical model for PTTD computed by using the original and modified PTHF correlations (Eqs. (18) and (19)) and the original decay coefficient (Eq. (28)). Note that although the decay coefficient will be modified by including the lower solid volume fraction PR-DNS data, we want to first examine the limitation of α_{PT} for which only the PTHF term has been modified. According to the figure, both PTTD models, derived from the original and modified PTHF, are not equal to zero when the solid volume fraction equals zero. For the PTTD in its original form, the value diverges to infinity as $\varepsilon_s \to 0$.

In order to address this problem, we propose the following argument. In the mathematical definition of PTTD (Eq. (29)) the denominator which contains the decay coefficient in terms of ε_s goes to zero as $\varepsilon_s \to 0$. In order to ensure that $\lim_{\varepsilon_s \to 0} \alpha_{PT}$ exists, the numerator must go to zero faster than the denominator as $\varepsilon_s \to 0$. In other words, a slower variation of the decay coefficient with $\varepsilon_s \to 0$, coupled with the exponential decay rate of PTHF, is necessary for specifying a zero limit of PTTD as solid volume fraction approaches zero.

Based on this analysis, the solid volume fraction ε_s in the decay coefficient λ_m has been replaced by a polynomial, in which the degree of the polynomial is chosen from an infinite geometric series $(1, 1/2, 1/4, \ldots)$ that converges absolutely. By fitting this polynomial to the PR-DNS data from $0.01 \le \varepsilon_s \le 0.5$ and $1 \le Re_m \le 100$, we find a new decay coefficient as follows

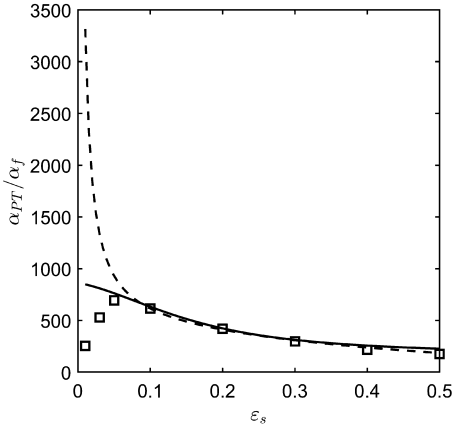

Fig. 6. Comparison of the PTTD model in the range $0.01 \le \varepsilon_s \le 0.03$ and $Re_m = 100$. The solid and dash lines represent the PTTD associated with Eqs. (18) and (19), respectively. The symbol represents the PTTD obtained from PR-DNS data. Note that the PTTD model is not vanishing as the solid volume fraction goes to zero.

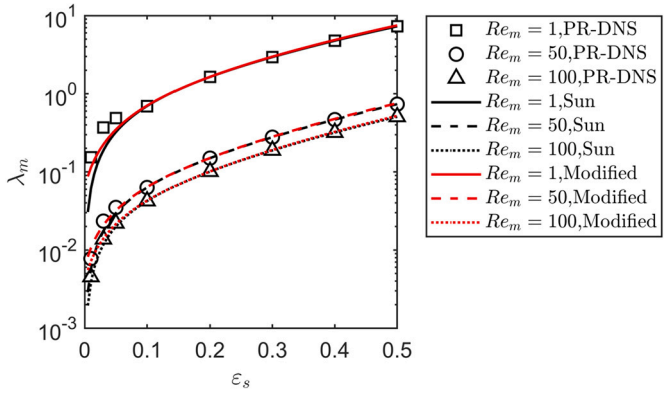

Fig. 7. Comparison of the non-dimensional decay coefficient in the range $0 \le \varepsilon_s \le 0.5$ and $1 \le Re_m \le 100$: symbols represent the decay coefficient obtained from PR-DNS data; black (original) and red (modified) lines represent decay coefficient.

$$\lambda_m = \frac{6\pi(1.17\varepsilon_s - 0.2021\varepsilon_s^{1/2} + 0.08568\varepsilon_s^{1/4})\langle Nu\rangle}{4(Re_m + 1.4)Pr}. \tag{30}$$

Fig. 7 compares the modified decay coefficient (Eq. (30)) to the original decay coefficient (Eq. (28)) with the PR-DNS result for different solid volume fraction and mean slip Reynolds number. It can be seen that both the original and modified decay coefficients are close to the PR-DNS results at higher solid volume fractions ($\varepsilon_s > 0.1$), which is to be expected. At lower solid volume fractions ($\varepsilon_s < 0.1$), the polynomial decay trend similar to that of the PTHF with decreasing solid volume fraction is observed in the λ_m values. However, near the lowest value of λ_m, the original decay coefficient decays much faster than the modified decay coefficient, indicating that the denominator may decay faster than the numerator in the PTTD expression (see Eq. (29)), eventually leading to blow-up of the PTTD correlation (Fig. 6). Through this analysis, it is safe to conclude that the prediction of the original decay coefficient at lower solid volume fractions is insufficient to determine the limiting value of PTTD. However, the modified decay coefficient overcomes this problem because of its slower decay rate, which still follows the PR-DNS result at lower solid volume fractions.

3.3. PTTD modification

The goal of modifying the PTHF correlation and the decay coefficient is to ensure that the derived PTTD correlation approaches zero as the solid volume fraction decreases to zero, which is not predicted by the previous study. Therefore, substituting the modified PTHF correlation (Eq. (19)) along with the modified decay coefficient (Eq. (30)) into the expression for the PTTD (Eq. (29)) results in the following expression

$$\frac{\alpha_{PT}}{\alpha_f} = \frac{2Re_m(Re_m + 1.4)Pr^2\exp(-0.002089Re_m)}{3\pi\langle Nu\rangle} \frac{(1-\varepsilon_s)(-5.11\varepsilon_s + 10.1\varepsilon_s^2 - 10.85\varepsilon_s^3) + 1 - \exp(-10.96\varepsilon_s)}{(1.17\varepsilon_s - 0.2021\varepsilon_s^{1/2} + 0.08568\varepsilon_s^{1/4})(1-\varepsilon_s)^2[1 - 1.6\varepsilon_s(1-\varepsilon_s) - 3\varepsilon_s(1-\varepsilon_s)^4\exp(-Re_m^{0.4}\varepsilon_s)]}. \tag{31}$$

To verify this model for the pseudo-turbulent thermal diffusivity α_{PT}, we compare Sun's correlation for α_{PT} and the PTTD data extracted from the PR-DNS simulations. Fig. 8 shows a comparison of the PTTD as a function of solid volume fraction at different Reynolds numbers. Overall, the modified PTTD, the original PTTD, and the PTTD from the PR-DNS simulations are in very good agreement for $\varepsilon_s > 0.1$. For lower solid volume fractions, particularly those at the edge of particle material fronts, the trend of polynomial decay in the PTTD gives a prediction based on the gradient-diffusion model, which is consistent with the numerical results from PR-DNS, whereas the original PTTD diverges.

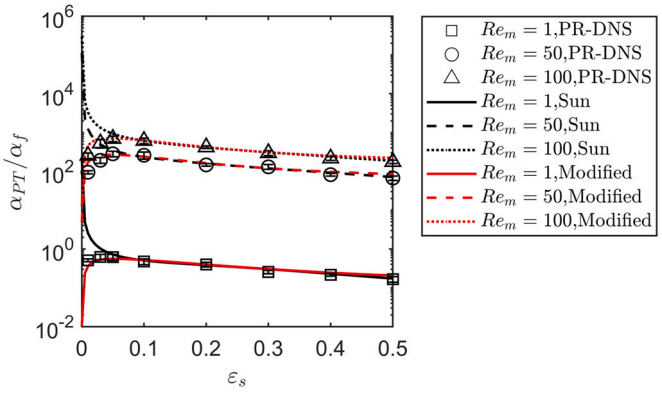

Fig. 8. Comparison of the pseudo-turbulent thermal diffusivity (PTTD) in the range $0 \le \varepsilon_s \le 0.5$ and $1 \le Re_m \le 100$: symbols represent the PTTD obtained from PR-DNS data; black (original) and red (modified) lines represent the PTTD correlation. Error bars represent 95% confidence intervals using 5 MIS.

3.4. Validity of closure models based on statistically homogeneous gas-solid flow

Here we discuss the validity of closure models developed from PR-DNS of a statistically homogeneous problem to practical applications that involve statistically inhomogeneous gas-solid flow. The central idea here is identical to how DNS of canonical flows such as homogeneous isotropic turbulence is used in single-phase turbulent flow to develop models for general inhomogeneous flows. Essentially we are assuming *local homogeneity* of the averaged flow fields such as average fluid and particle velocity and average solid volume fraction. This assumption holds when there is a separation of scales between the variation of these average quantities and the length scale associated with two-point correlations of pertinent fields.

In the hydrodynamic problem, statistically homogeneous gas-solid flow is simulated by establishing steady flow past statistically homogeneous random assemblies of stationary spherical particles in periodic domains (Tenneti et al., 2013). This problem has been thoroughly investigated and the validity of using ensemble-averaging of PR-DNS data from the statistically homogeneous flow fields to develop closure models, such as the drag law, for averaged Eulerian-Eulerian two-fluid (EE-TF) models has been rigorously established (Tenneti and Subramaniam, 2014; Mehrabadi et al., 2016). Several articles have also been

published on the heat transfer problem, and closure models for the average Nusselt number have been extracted from PR-DNS of a statistically homogeneous gas-solid flow using periodic boundary conditions for the development of EE TF models.

However, the validity of the closure models developed from PR-DNS is contingent upon the existence of scale separation: i.e., the characteristic length scale of macroscopic quantities is larger than that of mesoscale structures, which forms the basis for local closure models (Subramaniam, 2013). Sun (2016) validated the scale separation assumption by comparing the characteristic length scale of variation of mean quantities such as average bulk fluid temperature with a characteristic length scale from higher order statistics such as particle pair correlation or Eulerian two-point correlation of temperature and velocity. The length scale that characterizes the variation of average (nondimensional) bulk fluid temperature can be obtained by extracting the decay coefficient from the exponential decay model for the average bulk fluid temperature:

$$\langle \phi_m \rangle(x) = e^{-\lambda_m x/D}, \tag{32}$$

where λ_m is the non-dimensional decay coefficient. By fitting the PR-DNS data, a characteristic length scale can be defined as

$$\ell_{\langle \phi_m \rangle} = D/\lambda_m, \tag{33}$$

and it characterizes the variation of macroscopic average quantities. For the mesoscale, Sun et al. (2016) defined a two-point fluctuating velocity-(scaled) temperature correlation as follows:

$$\rho_{u_\parallel \theta}(\boldsymbol{r}) = \frac{\langle I_f(\boldsymbol{x})\theta''^{(f)}(\boldsymbol{x}) \cdot I_f(\boldsymbol{x}+\boldsymbol{r}) u_\parallel''^{(f)}(\boldsymbol{x}+\boldsymbol{r}) \rangle}{\langle I_f(\boldsymbol{x})\theta''^{(f)}(\boldsymbol{x}) \cdot I_f(\boldsymbol{x}) u_\parallel''^{(f)}(\boldsymbol{x}) \rangle}, \tag{34}$$

based on which the corresponding characteristic length scale can be defined as:

$$\ell_{u_\parallel \theta} = \int_0^\infty \rho_{u_\parallel \theta}(\boldsymbol{r}) d\boldsymbol{r}. \tag{35}$$

From PR-DNS of flow past a fixed bed of particles, it is found that $\ell_{u_\parallel \theta} \sim 3-4D$ (Sun et al., 2016). In other words, if $\ell_{\langle \phi_m \rangle} \geq \ell_{u_\parallel \theta}$, scale separation exists and the assumption of locally homogeneous mean fluid temperature is valid. If $\ell_{\langle \phi_m \rangle} < \ell_{u_\parallel \theta}$, the scale separation assumption ceases to be valid. In cases where the fluid is heated rapidly over a very short length scale by a dense bed of hot particles, the scale separation assumption breaks down and nonlocal closure models might be needed. Another situation where the scale separation assumption might break down is in cluster-induced turbulence where particles falling under gravity form large clusters on the order of hundreds of particle diameters. Without additional justification, it is not appropriate to use models based on PR-DNS of statistically homogeneous problems with periodic boundary conditions for these problems.

4. Conclusion

In order to address the issue of robust modeling of the PTHF near particle material fronts where the average solid volume fraction falls rapidly to zero, this study has extended the PR-DNS heat transfer simulation at steady flow past a random assembly of fixed, isothermal, monodisperse, spherical particles to low solid volume fractions (0.01-0.5) for a Prandtl number of 0.7 and mean slip Reynolds numbers in the range 1-100. The PR-DNS results indicate that the PTHF decays exponentially as the solid volume fraction approaches zero, which is physically reasonable and not predicted by Sun's PTHF correlation (Sun et al., 2016). At low volume fractions ($\varepsilon_s < 0.1$), Sun's correlation of PTHF encounters two problems. First, the non-zero limit of PTHF, during which the presence of particles is diminishing, is inevitable, causing inaccuracy in implementing the PTHF model in CFD simulations of two-fluid heat transfer, especially for dilute flow. Secondly, a discrepancy between Sun's correlation and the PR-DNS results was observed, indicating that Sun's correlation cannot capture the PTHF physics when $\varepsilon_s < 0.1$. In order to address these two problems, a modified correlation for the PTHF has been proposed. The original form of the PTTD approaches infinity as $\varepsilon_s \to 0$. In order to address this problem, an improved correlation for the decay coefficient of the mean fluid temperature has been developed.

Consequently, the modified PTTD decays polynomially as the solid volume fraction approaches zero, illustrating the extent of the transport of PTHF for $\varepsilon_s < 0.1$. Furthermore, the modified PTTD guarantees a zero limit at $\varepsilon_s = 0$, where, previously, the implementation of the original PTTD in two-fluid heat transfer was limited. Finally, the improved PTTD has already been tested by Peng et al. (2019) which yields stable results in inhomogeneous problems where the solid volume fraction approaches zero at the particle material fronts. As discussed in Appendix B, the neglect of free convection in obtaining these modifications to the PTHF and PTTD is valid for most of the Reynolds number regime, but free convection effects should be included when considering very low Reynolds number cases in certain applications such as fast pyrolysis of biomass or CO_2 capture using dry sorbent particles.

Declaration of competing interest

The authors declare that they have no known competing financial interests or personal relationships that could have appeared to influence the work reported in this paper.

Data availability

Data will be made available on request.

Acknowledgements

This work was supported by the National Science Foundation [grant number 1905017].

Appendix A. Verification of the isothermal particle assumption

We discuss the validity of the isothermal boundary condition in the following. The most general boundary condition at the particle-fluid interface is continuity of the temperature and the heat flux at the interface. This requires a fully coupled solution of the temperature equation in the particle and fluid phases, given by

$$\frac{\partial T_s}{\partial t} = \alpha_s \nabla^2 T_s \tag{A.1a}$$

$$\frac{\partial T_f}{\partial t} + \boldsymbol{u} \cdot \nabla T_f = \alpha_f \nabla^2 T_f, \tag{A.1b}$$

where the subscripts 's' and 'f' refer to the particle and fluid phases, respectively. At every point on the particle-fluid interface the boundary conditions require:

$$T_s(\boldsymbol{x}, t) = T_f(\boldsymbol{x}, t) \tag{A.2}$$

$$-k_s \boldsymbol{n} \cdot \nabla T_s(\boldsymbol{x}, t) = -k_f \boldsymbol{n} \cdot \nabla T_f(\boldsymbol{x}, t), \tag{A.3}$$

where k_s and k_f are the thermal conductivity in the particle and fluid phases, respectively, and $\boldsymbol{n}$ is the outward unit normal to the particle.

This coupled solution is expensive and unnecessary if the temperature field inside the particle is uniform, which holds if the Biot number $Bi = hD/k_s$ is small (usually it is required that $Bi \ll 1$, but $Bi \leq 0.1$ is deemed sufficient). The Biot number depends on the convective heat transfer coefficient h, the particle diameter D, and the thermal conductivity of the particle k_s. For the target applications the particle diameter is usually quite small (100-400 μm) (see Table A.2) and it is worth checking if this simplifying assumption is valid. Substituting for the convective heat transfer coefficient h in terms of the Nusselt number using $h = k_f Nu/D$, we obtain $Bi = Nu(k_f/k_s)$. Unfortunately the

Table A.2
Typical particle properties encountered in gas-solid heat transfer applications such as CO2 capture (Yi et al. (2007)), biomass pyrolysis (Xue et al. (2011)), and chemical looping combustion (CLC) (Shen et al. (2008)). The gas and solid phase for each gas-solid heat transfer application are: CO_2 and $NaCO_3$ in CO_2 capture; N_2 and bagasse in biomass pyrolysis; CO and $CaSO_4$ in CLC. The Biot number is computed as $Bi = Nu(k_f/k_s)$ for Nusselt number values in the range 2 to 10.

	k_s(W/m · K)	k_f(W/m · K)	k_s/k_f	$\rho_s c_{ps}/\rho_f c_{pf}$	$D(\mu$m)	Bi
CO_2 capture	0.5	0.017	30	6254	404	0.067 ; 0.33
Biomass	0.6	0.054	11	1772	500	0.182 ; 0.91
CLC	0.9	0.052	17	12843	100	0.118 ; 0.59

Biot number criterion for uniform particle temperature cannot be verified *a priori* because it involves the Nusselt number corresponding to gas–solid heat transfer, which is the output of the PR-DNS. As an *a posteriori* justification, taking the range of Nusselt number from Sun et al. (2015) we estimate the range of Biot number to be 0.067-0.91. These simple estimates indicate that for lower values of the Nusselt number ($2 < Nu < 10$), the Biot number criterion indicates that the particle temperature is fairly uniform for the lower limit of the Nusselt number, but this may not hold for higher Nusselt number values ($Nu > 10$), especially for the biomass and CLC applications.

If the Biot number is small, the lumped capacitance analysis holds and we can solve for the volume-averaged temperature of the particle $\overline{T}_s$, which is assumed to be uniform inside the particle. In this case the general boundary conditions at the particle-fluid interface simplify to

$$\overline{T}_s(t) = T_f(\boldsymbol{x}, t) \tag{A.4}$$

$$\rho_s c_{p,s} V_s \frac{\partial \overline{T}_s(t)}{\partial t} = -\int_{A_s} k_f \, \boldsymbol{n} \cdot \boldsymbol{\nabla} T_f(\boldsymbol{x}, t) \, dA_s, \tag{A.5}$$

where V_s is the particle volume and A_s is the particle surface area. Note that although the particle and fluid solutions are still coupled, the particle temperature equation is now an ordinary differential equation which is much simpler to solve.

If the time scale of evolution of the volume-averaged particle temperature in the lumped capacitance model is very large compared to the time it takes for the Nusselt number to reach a steady value in the PR-DNS, then we can assume an isothermal particle that has a uniform temperature field that does not vary in time. In this case the boundary conditions at the particle-fluid interface simplify to

$$\overline{T}_s = T_f(\boldsymbol{x}, t), \tag{A.6}$$

which is the boundary condition used in the PR-DNS results presented in this paper. This boundary condition has the additional advantage of allowing the thermally fully developed condition to be satisfied in the periodic domain setup of the problem. Note that in the PR-DNS results shown in this paper a steady fluid velocity field is taken from a prior hydrodynamic simulation. The thermally fully developed formulation in a periodic domain has not been tested for a time–varying particle temperature that is coupled to an evolving fluid velocity field.

We have performed simulations with time–varying particle temperature using a different PUReIBM setup, which provide justification for our assumption of isothermal particles. Sun (2016) developed a fully finite-difference (FFD) PUReIBM implementation that extends the work of Garg et al. (2011) and Tenneti et al. (2010, 2011, 2013) who developed the pseudo-spectral (PS) implementation of PUReIBM to simulate gas-solid flow by imposing periodic boundary conditions. With the FFD PUReIBM implementation, it is possible to simulate a time-varying particle temperature boundary condition (cf. Eq. (A.4)), and to also impose inflow/outflow boundary conditions in the streamwise direction, while wall boundary conditions can be imposed in the cross-stream directions. Thus FFD PUReIBM enables simulations of transient heat transfer from a sphere in a duct flow.

Fig. A.9 shows the time history of the non-dimensional particle temperature φ_s for different particle-to-fluid thermal inertia ratios at the same particle Reynolds number (100) based on Prandtl number (0.7). The inlet condition corresponds to a uniform velocity U_∞ and temperature T_∞.

The non-dimensional temperature is defined as $\varphi = (T - T_\infty)/(T_{s,i} - T_\infty)$, where $T_{s,i}$ is the initial particle temperature and T_∞ is the inlet flow temperature.[1] The evolution equations for non-dimensional particle and fluid temperature corresponding to the dimensional equations (see Eq. (A.1)) presented earlier are:

$$\frac{\partial \varphi_s}{\partial \tau} = \frac{1}{Pe} \frac{\alpha_s}{\alpha_f} \bar{\nabla}^2 \varphi_s \tag{A.7a}$$

$$\frac{\partial \varphi_f}{\partial \tau} + \boldsymbol{U} \cdot \bar{\nabla} \varphi_f = \frac{1}{Pe} \bar{\nabla}^2 \varphi_f \tag{A.7b}$$

where the Peclet number $Pe = Re_D Pr$ characterizes the ratio of the convective time scale and the diffusion time scale inside flow, and $\bar{\nabla} = D\nabla$. The lumped capacitance model is obtained by integrating the particle temperature over a spherical volume region V_s to obtain the non-dimensional volume–averaged particle temperature $\bar{\varphi}_s$, which is purely time-dependent $\bar{\varphi}_s(t)$, and evolves by

$$\int_{V_s} \frac{\partial \varphi_s}{\partial \tau} \, dV_s = V_s \frac{d\bar{\varphi}_s}{d\tau} = \frac{1}{Pe} \frac{\alpha_s}{\alpha_f} \int_{A_s} \bar{\nabla} \varphi_s \cdot \boldsymbol{n} dA_s, \tag{A.8}$$

where $\tau = tU_\infty/D$. Since the heat flux at the interface between the solid and fluid phases is continuous, the total heat transfer from solid to fluid can be expressed as:

$$-\int_{A_s} k_s \bar{\nabla} \varphi_s \cdot \boldsymbol{n} dA_s = -\int_{A_s} k_f \bar{\nabla} \varphi_f \cdot \boldsymbol{n} dA_s. \tag{A.9}$$

Therefore, the total heat transfer $\int_{A_s} k_f \bar{\nabla} \varphi_f \cdot \boldsymbol{n} dA_s$ can be computed from the gradient of fluid temperature.

The non-dimensional inlet temperature is $\varphi_\infty = 0$. The temperature of the duct wall is the same as the initial sphere temperature, such that $\varphi_{wall} = 1$ and is constant in time and space. The height of the duct is $3D$ and the length of the duct is $10D$. The fixed sphere is located in the center of the duct, and its initial temperature is set to $\varphi_{s,i} = 1$. Once the flow and temperature fields reach steady-state, the sphere temperature is allowed to evolve in time according to Eq. (A.8).

Figs. A.9(a) and (b) show that the non-dimensional particle temperature is practically constant over the time interval that the Nusselt number reaches its steady value. Note that all the target applications have thermal inertia ratios between cases (a) and (b). In Fig. A.9(c) for a lower thermal inertia ratio, the non-dimensional particle temperature decreases significantly with time, while the average Nusselt number ($Nu = hD/k_f$, where h is the average heat transfer coefficient) decreases more rapidly and approaches an asymptotic value relatively quickly for $\tau \geq 1$. These trends are similar to those found in other works (Feng and Michaelides, 2000; Balachandar and Ha, 2001) for unbounded flow past a sphere at $Pr = 0.7$ for different particle Reynolds numbers. Note that for $\rho_s c_{ps}/\rho_f c_{pf} = 1000$ and 2000, the non-dimensional particle temperature decreases $< 10\%$ when the thermally

[1] Note that in the appendix, a different set of reference variables is used to defining the non-dimensional temperature, and its symbol is also different.

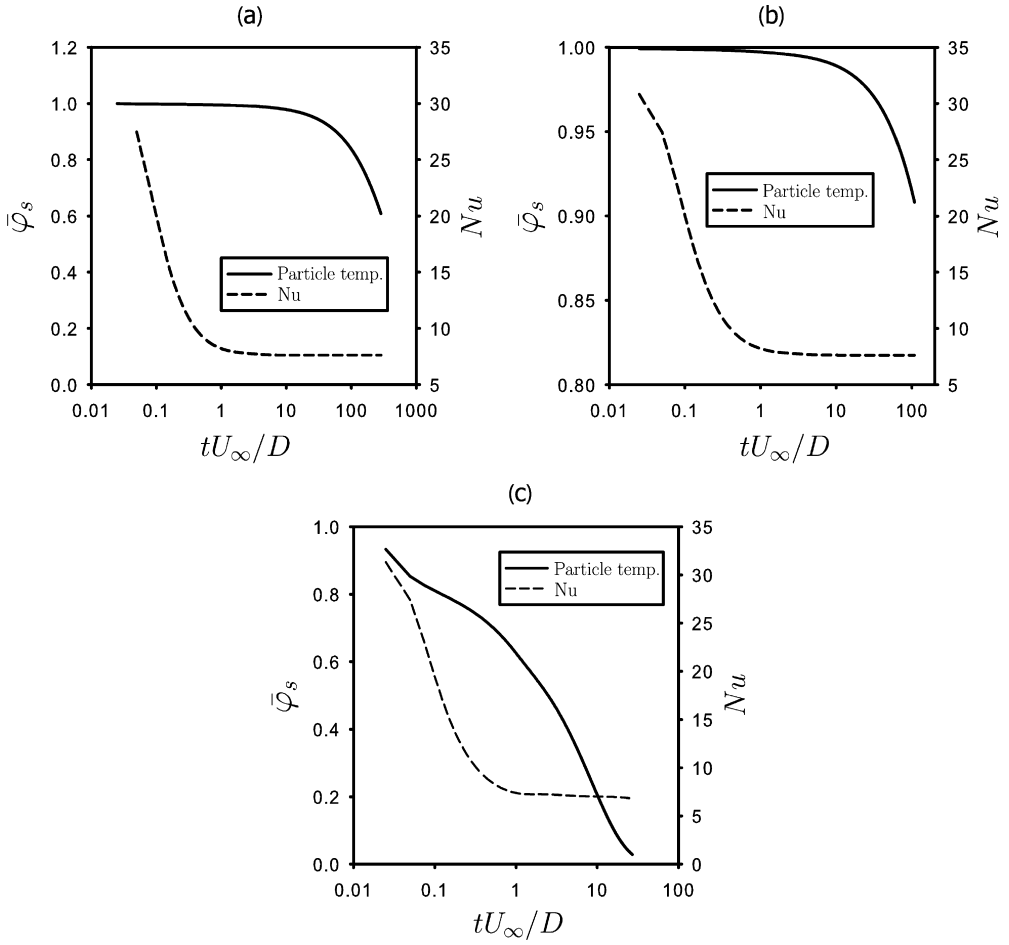

Fig. A.9. Time history of non-dimensional sphere temperature φ_s and Nusselt number for the particle-to-fluid thermal inertia ratio $\rho_s c_{ps}/\rho_f c_{pf}$ equal to (a) 1000, (b) 2000, and (c) 10. The solid lines represent the non-dimensional sphere temperature and the dashed lines represent the average Nusselt number. U_∞ is the uniform inlet velocity.

Table A.3
Ratios of thermal time scales from typical particle properties encountered in gas-solid heat transfer applications. There are four timescales: (1) the conduction timescale in the solid phase $\tau_s = D^2/\alpha_s$, (2) the conduction timescale in the fluid phase $\tau_f = D^2/\alpha_f$, (3) the convection timescale in the fluid phase $\tau_c = D/U_\infty$, and (4) the timescale of interphase heat transfer $\tau_{pf} = V_s \rho_s c_{ps}/hA_s$. The timescale ratios are computed for Nusselt number values in the range 2 to 10 and for Péclet number of 70 (corresponding to heat transfer from a particle in air at a Reynolds number of 100).

	$\frac{\tau_{pf}}{\tau_s} = \frac{k_s}{6Nuk_f} = \frac{1}{6Bi}$	$\frac{\tau_{pf}}{\tau_f} = \frac{\rho_s c_{ps}}{6Nu\rho_f c_{pf}}$	$\frac{\tau_{pf}}{\tau_c} = \frac{Pe\rho_s c_{ps}}{6Nu\rho_f c_{pf}}$	$\frac{\tau_s}{\tau_f} = \frac{\alpha_f}{\alpha_s}$
CO_2 capture	0.50 ; 2.50	104 ; 521	7280 ; 36470	208
Biomass	0.18 ; 0.92	30 ; 148	2100 ; 10360	161
CLC	0.28 ; 1.42	214 ; 1070	14980 ; 74900	755

fully developed flow is reached (Nusselt number goes to an asymptotic value at $\tau \approx 1$).

This is because the convective timescale of the flow $\tau_c = D/U_\infty$ is far less than the characteristic timescale of the interphase heat transfer defined as $\tau_{pf} = V_s \rho_s c_{ps}/hA_s$, that is, $\tau_{pf}/\tau_c = \rho_s c_{ps} V_s PrRe_D/\rho_f c_{pf} DA_s Nu > 5000$ for $\rho_s c_{ps}/\rho_f c_{pf} > 1000$ and $Re_D = 100$. Table A.3 lists the principal time scales involved in the gas-solid heat transfer problem. In other words, the timescale at which the Nusselt number reaches steady-state is much smaller than the timescale for interphase heat transfer. Therefore, there exists a finite time interval during which the variation of the particle temperature is negligible while the average Nusselt number has reached steady-state. This justifies the use of a time–independent temperature boundary condition in the paper.

By assuming a lumped capacitance model, Sun (2016) demonstrated the temporal uniformity of the particle temperature for $\rho_s c_{ps}/\rho_f c_{pf} > 1000$ and $Re_D = 100$, which is relevant to practical gas-solid systems. However, the spatial uniformity of temperature inside the particle, which is the second necessary condition for the isothermal particle assumption, is yet to be confirmed.

Zhou (2022) considered the free thermal evolution of a spherical particle subjected to a non-isothermal stagnant flow and developed a one-dimensional (1D) numerical model in spherical coordinates to investigate the thermal history along the radial direction. This is essentially solving a coupled heat conduction problem in both solid and fluid phases. The evolution equations of non-dimensional particle and fluid temperature (see Eq. (A.7)) can be simplified as follows:

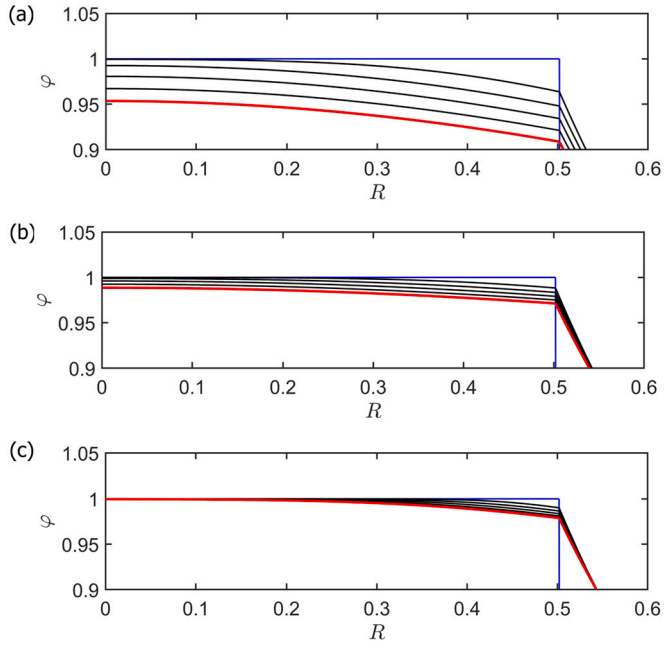

Fig. A.10. Time history of non-dimensional temperature φ inside the particle ($0 \le R \le 0.5$) for (a) biomass pyrolysis, (b) CO_2 capture, and (c) chemical looping combustion. Black lines represent the consecutive solutions with the time step $\Delta\tau = 2\tau_f$, while the blue line is the solution at the initial condition at $\tau = 0$ and red is the final solution at $\tau = 10\tau_f$, where $\tau_f = D^2/\alpha_f$ is the conduction timescale in the fluid phase.

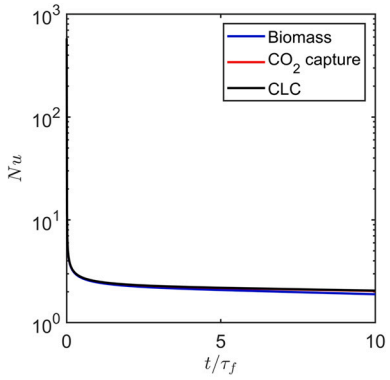

Fig. A.11. Time history of the Nusselt number for various types of gas-solid particles obtained from the 1D numerical model of coupled conduction in both phases.

$$\frac{\partial \varphi_s}{\partial \tau} = \frac{\alpha_s}{\alpha_f}\frac{1}{R^2}\frac{\partial}{\partial R}\left(R^2\frac{\partial \varphi_s}{\partial R}\right) \tag{A.10a}$$

$$\frac{\partial \varphi_f}{\partial \tau} = \frac{1}{R^2}\frac{\partial}{\partial R}\left(R^2\frac{\partial \varphi_f}{\partial R}\right) \tag{A.10b}$$

where $R = r/D$ is the non-dimensional space in the radial direction, with $R = 0.5$ and $R = 5$ being the particle-fluid interface and the far flow field, respectively. The above two equations need to be solved together along with the boundary conditions of $\partial\varphi/\partial R = 0$ at $R = 0$ and $R = 5$, and the continuity condition of temperature and heat flux applied at the particle-fluid interface given by

$$\varphi_s = \varphi_f \tag{A.11a}$$

$$k_s\frac{d\varphi_s}{dR} = -k_f\frac{d\varphi_f}{dR} \tag{A.11b}$$

The initial conditions are identical to the lumped capacitance model.

Fig. A.10 shows the time history of non-dimensional temperature φ for the particles listed in Table A.2. Several important observations can be made. Firstly, the non-dimensional temperature decreases less than 10% at the particle surface over the time it takes for the Nusselt number to reach its asymptotic value at $\tau \approx 1$ as shown in Fig. A.11. This is because the conduction timescale in the fluid phase is much less than the characteristic timescale of the interphase heat transfer, i.e., $\tau_{pf}/\tau_f = \rho_s c_{ps} V_s/\rho_f c_{pf} A_s DNu \sim O(10^2)$ for the thermal inertia ratio of the biomass particle ($\rho_s c_{ps}/\rho_f c_{pf} = 1772$) and $Nu = 2$ (see Table A.3).

Furthermore, the temperature distribution inside the particle exhibits non-uniformity. This is because the conduction timescale in the solid phase is much larger than the conduction timescale in the fluid phase, i.e., $\tau_s/\tau_f = \alpha_f/\alpha_s = k_f\rho_s c_{ps}/k_s\rho_f c_{pf} \sim O(10^2)$ for the particles in gas-solid flow that are listed in Table A.3. Such a large separation between τ_s and τ_f can result in a finite time interval during which the conduction in the solid phase is negligible while the Nusselt number has reached a quasi-steady value. Although this argument is true for the pure conduction problem where $Nu = 2$, it does not guarantee a spatially uniform temperature distribution in the solid phase for the convection problem considered in the PR-DNS. This is because the criterion for negligible spatial variation of the particle temperature inside the solid in convective heat transfer is that the ratio of the interphase heat transfer time scaleτ_{pf} to the conduction in the solid phase τ_s be large. This ratio $\tau_{pf}/\tau_s = k_s/6Nuk_f$ significantly decreases for higher Nusselt number values, because it is inversely proportional to the Nusselt number. However, for lower Nusselt number values ranging from 2-10 and Péclet number of 70, we find that the conduction timescale in the solid phase is comparable to the timescale of the interphase heat transfer (see Table A.3). Since the highest Nusselt number values encountered in the PR-DNS simulations (Sun et al., 2015) is less than 15, the isothermal particle assumption with a time-independent, near-uniform temperature inside the particle is justified for the target applications considered. Table A.3 also indicates that the order of the thermal timescales for these applications at sufficiently high Reynolds number is $\tau_c \ll \tau_f \ll \tau_s \approx \tau_{pf}$.

Appendix B. Verification of the free convection assumption

For a spherical particle of diameter D at temperature T_s placed in air at temperature T_f, free convection is characterized by the Grashof number which is defined by

$$Gr = \frac{g\beta(T_f - T_s)D^3}{\nu_f^2}, \tag{B.1}$$

where β is the volumetric thermal expansion coefficient ($\beta = 1/T_f$ for isobaric expansion in ideal gases), and g is the acceleration due to gravity. Free convection effects can be neglected if the ratio of the Grashof number to the square of the Reynolds number is much less than one ($Gr/Re_m^2 \ll 1$). For each Reynolds number, this constraint imposes an upper limit on the particle diameter above which free convection effects cannot be neglected. In other words, for a given value of T_f/T_s, the upper limit on the particle diameter D increases with increasing Reynolds number. Considering a typical fluid-to-solid temperature ratio of $T_f/T_s = 5$, assuming air as the fluid under terrestrial conditions ($g = 9.81$ m/s^2) and applying the constraint of $Gr/Re_m^2 \le 0.01$, we calculate the maximum particle diameter $D_{max} = [0.01Re_m^2\nu_f^2/g\beta(T_f - T_s)]^{1/3}$ for which free convection can be neglected ($Gr/Re_m^2 \ll 1$) over the range of Reynolds number ($1 \le Re_m \le 100$). Fig. B.12 shows that the upper limit on the particle diameter D_{max} increases with increasing Reynolds

Table B.4
The minimum Reynolds number of gas-solid particles for neglecting free convection. The criterion of the Reynolds number is computed from $Gr/Re_m^2 \le 0.01$, where $Gr = g\beta(T_f - T_s)D^3/\nu_f^2$. The fluid-to-solid temperature ratio is taken as $T_f/T_s = 5$ and air is chosen to be the fluid phase under terrestrial condition. The kinematic viscosity of air is selected based on different gas-solid heat transfer conditions: 2.3×10^{-5} m^2/s (Biomass), 7×10^{-5} m^2/s (CO_2 capture), and 1.72×10^{-4} m^2/s (CLC).

	$D(\mu m)$	$Re_{m,min}$
CO_2 capture	404	3.25
Biomass	500	13.62
CLC	100	0.16

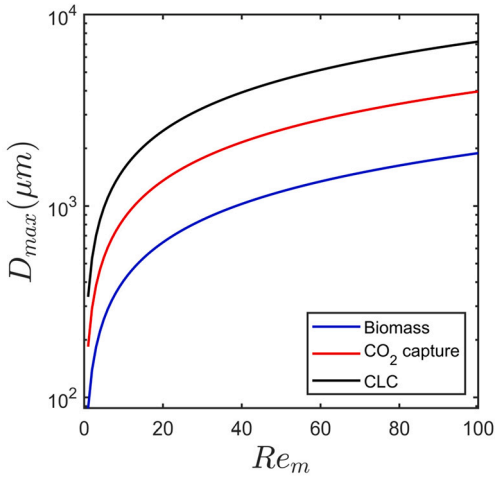

Fig. B.12. The maximum particle diameter of the gas-solid heat transfer for neglecting free convection. The criterion of the particle diameter is computed from $Gr/Re_m^2 \le 0.01$, where $Gr = g\beta(T_f - T_s)D^3/\nu_f^2$. The fluid-to-solid temperature ratio is taken as $T_f/T_s = 5$ and air is chosen to be the fluid phase under terrestrial condition. The kinematic viscosity of air is selected based on different gas-solid heat transfer conditions: 2.3×10^{-5} m^2/s (Biomass), 7×10^{-5} m^2/s (CO_2 capture), and 1.72×10^{-4} m^2/s (CLC).

number, indicating that the upper limit of D for neglecting free convection is less restrictive at high Reynolds number cases where forced convection dominates. However, the upper limit on the particle diameter is more restrictive for lower Reynolds number cases. For instance, the particle diameter has to be less than 88 μm in order to neglect free convection at $Re_m = 1$. Furthermore, we estimate the minimum Reynolds number ($Re_{m,min} = [g\beta(T_f - T_s)D^3/0.01\nu_f^2]^{1/2}$) that is required for negligible free convection if the particle diameter D is given. Table B.4 summarizes the minimum Reynolds numbers of typical gas-solid particles allowed for neglecting free convection. The results show that the minimum Reynolds numbers are outside the Stokes flow regime, suggesting that the free convection effects could become an important factor affecting the velocity and temperature fluctuations, particularly when the flow past particles is laminar and approaching Stokes regime.

Although the current PR-DNS has not yet explored the influence of the free convection on the behavior of PTHF, it is appropriate to use the current PTHF model by assuming negligible free convection based on the ratio of $Gr/Re_m^2 \ll 1$ with physical properties for a specific heat transfer problem, which applies to many situations for typical biomass particles outside small Reynolds number flow. For low Reynolds number flow, the PTHF model, developed under the assumption of negligible free convection, needs to be re-evaluated in practical applications, such as those involving CO_2 capture by dry sorbents and fast pyrolysis of biomass (see Table B.5).

Table B.5
The ratio of the Grashof number to the square of the Reynolds number in different PR-DNS cases (Re_m and ε_s are varying) with practical applications in fast pyrolysis of biomass, CO_2 capture using dry particle sorbents, and chemical looping combustion (CLC). The calculation conditions of Gr/Re_m^2, where $Gr = g\beta(T_f - T_s)D^3/\nu_f^2$, are as follows: (a) The fluid-to-solid temperature ratio is taken as $T_f/T_s = 5$. (b) Air is chosen to be the fluid phase under terrestrial conditions, and the kinematic viscosity of air is selected based on different gas-solid heat transfer conditions: 2.3×10^{-5} m^2/s (Biomass), 7×10^{-5} m^2/s (CO_2 capture), and 1.72×10^{-4} m^2/s (CLC). (c) The particle diameter D is 500 μm (Biomass), 404 μm (CO_2 capture), and 100 μm (CLC). At $Re_m = 1$, both CO_2 sorbent and biomass cases violate the criterion of $Gr/Re_m^2 \le 0.01$ (highlighted in gray cells).

		$Re_m = 1$	$Re_m = 50$	$Re_m = 100$
CO_2	$\varepsilon_s = 0.01$	0.1056	4.22×10^{-5}	1.06×10^{-5}
	$\varepsilon_s = 0.03$	0.1056	4.22×10^{-5}	1.06×10^{-5}
	$\varepsilon_s = 0.05$	0.1056	4.22×10^{-5}	1.06×10^{-5}
	$\varepsilon_s = 0.1$	0.1056	4.22×10^{-5}	1.06×10^{-5}
	$\varepsilon_s = 0.2$	0.1056	4.22×10^{-5}	1.06×10^{-5}
	$\varepsilon_s = 0.3$	0.1056	4.22×10^{-5}	1.06×10^{-5}
	$\varepsilon_s = 0.4$	0.1056	4.22×10^{-5}	1.06×10^{-5}
	$\varepsilon_s = 0.5$	0.1056	4.22×10^{-5}	1.06×10^{-5}
Biomass	$\varepsilon_s = 0.01$	1.8544	7.42×10^{-4}	1.85×10^{-4}
	$\varepsilon_s = 0.03$	1.8544	7.42×10^{-4}	1.85×10^{-4}
	$\varepsilon_s = 0.05$	1.8544	7.42×10^{-4}	1.85×10^{-4}
	$\varepsilon_s = 0.1$	1.8544	7.42×10^{-4}	1.85×10^{-4}
	$\varepsilon_s = 0.2$	1.8544	7.42×10^{-4}	1.85×10^{-4}
	$\varepsilon_s = 0.3$	1.8544	7.42×10^{-4}	1.85×10^{-4}
	$\varepsilon_s = 0.4$	1.8544	7.42×10^{-4}	1.85×10^{-4}
	$\varepsilon_s = 0.5$	1.8544	7.42×10^{-4}	1.85×10^{-4}
CLC	$\varepsilon_s = 0.01$	2.65×10^{-4}	1.06×10^{-7}	2.65×10^{-8}
	$\varepsilon_s = 0.03$	2.65×10^{-4}	1.06×10^{-7}	2.65×10^{-8}
	$\varepsilon_s = 0.05$	2.65×10^{-4}	1.06×10^{-7}	2.65×10^{-8}
	$\varepsilon_s = 0.1$	2.65×10^{-4}	1.06×10^{-7}	2.65×10^{-8}
	$\varepsilon_s = 0.2$	2.65×10^{-4}	1.06×10^{-7}	2.65×10^{-8}
	$\varepsilon_s = 0.3$	2.65×10^{-4}	1.06×10^{-7}	2.65×10^{-8}
	$\varepsilon_s = 0.4$	2.65×10^{-4}	1.06×10^{-7}	2.65×10^{-8}
	$\varepsilon_s = 0.5$	2.65×10^{-4}	1.06×10^{-7}	2.65×10^{-8}

References

Abanades, J.C., Anthony, E.J., Lu, D.Y., Salvador, C., Alvarez, D., 2004. Capture of CO_2 from combustion gases in a fluidized bed of CaO. AIChE J. 50, 1614–1622.

Balachandar, S., Ha, M., 2001. Unsteady heat transfer from a sphere in a uniform cross-flow. Phys. Fluids 13, 3714–3728.

Boateng, A., Mtui, P., 2012. CFD modeling of space-time evolution of fast pyrolysis products in a bench-scale fluidized-bed reactor. Appl. Therm. Eng. 33, 190–198.

Drew, D.A., 1983. Mathematical modeling of two-phase flow. Annu. Rev. Fluid Mech. 15, 261–291.

Feng, Z.G., Michaelides, E.E., 2000. A numerical study on the transient heat transfer from a sphere at high Reynolds and Peclet numbers. Int. J. Heat Mass Transf. 43, 219–229.

Fox, R.O., 2003. Computational Models for Turbulent Reacting Flows. Cambridge University Press.

Garg, R., 2009. Modeling and Simulation of Two-Phase Flows. Iowa State University.

Garg, R., Tenneti, S., Yusof, J.M., Subramaniam, S., 2011. Direct numerical simulation of gas-solids flow based on the immersed boundary method. In: Computational Gas-Solids Flows and Reacting Systems: Theory, Methods and Practice. IGI Global, pp. 245–276.

Mehrabadi, M., Murphy, E., Subramaniam, S., 2016. Development of a gas–solid drag law for clustered particles using particle-resolved direct numerical simulation. Chem. Eng. Sci. 152, 199–212.

Mehrabadi, M., Tenneti, S., Garg, R., Subramaniam, S., 2015. Pseudo-turbulent gas-phase velocity fluctuations in homogeneous gas-solid flow: fixed particle assemblies and freely evolving suspensions. J. Fluid Mech. 770, 210–246.

Papadikis, K., Gu, S., Bridgwater, A.V., 2009. CFD modelling of the fast pyrolysis of biomass in fluidised bed reactors: modelling the impact of biomass shrinkage. Chem. Eng. J. 149, 417–427.

Peng, C., Kong, B., Zhou, J., Sun, B., Passalacqua, A., Subramaniam, S., Fox, R.O., 2019. Implementation of pseudo-turbulence closures in an Eulerian-Eulerian two-fluid model for non-isothermal gas-solid flow. Chem. Eng. Sci. 207, 663–671.

Pope, S.B., 2000. Turbulent Flows. Cambridge University Press.

Shen, L., Zheng, M., Xiao, J., Xiao, R., 2008. A mechanistic investigation of a calcium-based oxygen carrier for chemical looping combustion. Combust. Flame 154, 489–506.

Shukla, P.R., Skeg, J., Buendia, E.C., Masson-Delmotte, V., Pörtner, H., Roberts, D., Zhai, P., Slade, R., Connors, S., van Diemen, S., et al., 2019. Climate change and land: an ipcc special report on climate change, desertification, land degradation, sustainable land management, food security, and greenhouse gas fluxes in terrestrial ecosystems.

Subramaniam, S., 2013. Lagrangian–Eulerian methods for multiphase flows. Prog. Energy Combust. Sci. 39, 215–245.

Sun, B., 2016. Modeling heat and mass transfer in reacting gas-solid flow using particle-resolved direct numerical simulation. Ph.D. thesis. Iowa State University.

Sun, B., Tenneti, S., Subramaniam, S., 2015. Modeling average gas-solid heat transfer using particle-resolved direct numerical simulation. Int. J. Heat Mass Transf. 86, 898–913.

Sun, B., Tenneti, S., Subramaniam, S., Koch, D.L., 2016. Pseudo-turbulent heat flux and average gas-phase conduction during gas-solid heat transfer: flow past random fixed particle assemblies. J. Fluid Mech. 798, 299–349.

Syamlal, M., Rogers, W., O'Brien, T.J., 1993. MFIX documentation theory guide. Technical Report. USDOE Morgantown Energy Technology Center, WV (United States).

Tavassoli, H., Kriebitzsch, S., Van der Hoef, M., Peters, E., Kuipers, J., 2013. Direct numerical simulation of particulate flow with heat transfer. Int. J. Multiph. Flow 57, 29–37.

Tenneti, S., Garg, R., Hrenya, C., Fox, R., Subramaniam, S., 2010. Direct numerical simulation of gas–solid suspensions at moderate Reynolds number: quantifying the coupling between hydrodynamic forces and particle velocity fluctuations. Powder Technol. 203, 57–69.

Tenneti, S., Garg, R., Subramaniam, S., 2011. Drag law for monodisperse gas–solid systems using particle-resolved direct numerical simulation of flow past fixed assemblies of spheres. Int. J. Multiph. Flow 37, 1072–1092.

Tenneti, S., Subramaniam, S., 2014. Particle-resolved direct numerical simulation for gas-solid flow model development. Annu. Rev. Fluid Mech. 46, 199–230.

Tenneti, S., Sun, B., Garg, R., Subramaniam, S., 2013. Role of fluid heating in dense gas-solid flow as revealed by particle-resolved direct numerical simulation. Int. J. Heat Mass Transf. 58, 471–479.

Xue, Q., Heindel, T., Fox, R., 2011. A CFD model for biomass fast pyrolysis in fluidized-bed reactors. Chem. Eng. Sci. 66, 2440–2452.

Yi, C.K., Jo, S.H., Seo, Y., Lee, J.B., Ryu, C.K., 2007. Continuous operation of the potassium-based dry sorbent CO_2 capture process with two fluidized-bed reactors. Int. J. Greenh. Gas Control 1, 31–36.

Zhou, J., 2022. Developing models for gas-solid heat transfer using particle-resolved direct numerical simulation. Master's thesis. Iowa State University.